



# NH<sub>2</sub>-MIL-125(Ti)/TiO<sub>2</sub> nanorod heterojunction photoanodes for efficient photoelectrochemical water splitting

Ji Won Yoon<sup>a</sup>, Do Hong Kim<sup>a</sup>, Jae-Hyeok Kim<sup>a</sup>, Ho Won Jang<sup>b</sup>, Jong-Heun Lee<sup>a,\*</sup>

<sup>a</sup> Department of Materials Science Engineering, Korea University, Seoul, 02841, Republic of Korea

<sup>b</sup> Department of Materials Science and Engineering, Research Institute of Advanced Materials, Seoul National University, Seoul, 08826, Republic of Korea

## ARTICLE INFO

### Keywords:

Hydrothermal reaction  
Photoelectrochemical water splitting  
Photoanode  
TiO<sub>2</sub> nanorod  
MIL(125)-NH<sub>2</sub>

## ABSTRACT

A photoactive amine-functionalized Ti metal-organic framework (MOF) (MIL(125)-NH<sub>2</sub>(Ti)) layer is uniformly coated on vertically ordered TiO<sub>2</sub> nanorods (NRs) via a facile hydrothermal reaction, and the performance of the heterojunction photoanode in photoelectrochemical (PEC) water splitting is studied. The photocurrent density of the MIL(125)-NH<sub>2</sub>/TiO<sub>2</sub> NRs reaches 1.63 mA/cm<sup>2</sup> at 1.23 V vs. a reversible hydrogen electrode under AM 1.5 G simulated sunlight illumination, which is ~2.7 times higher than that of pristine TiO<sub>2</sub> NRs. The incident photon-to-electron conversion efficiency of the MIL(125)-NH<sub>2</sub>/TiO<sub>2</sub> NRs improves significantly at  $\lambda_{\text{max}} = 340$  nm, implying the promotion of water oxidation through efficient light absorption and charge separation. The enhancement of the PEC activity in the TiO<sub>2</sub> NRs caused by an MIL(125)-NH<sub>2</sub> coating is discussed in relation to the surface area and elongated configuration of the TiO<sub>2</sub> NRs, the band gap of MIL(125)-NH<sub>2</sub>(Ti), and the type (II) heterojunction. This study demonstrates the rational design of heterojunctions between the semiconductor and the MOF, which paves the way for new facile and general approaches to achieve a high efficiency in water splitting.

## 1. Introduction

Hydrogen is an environmentally friendly and viable alternative to fossil fuels. One of the most effective and clean routes to harvest hydrogen is sunlight-activated photoelectrolysis. Remarkable efforts have been directed towards achieving efficient water splitting with photoelectrochemical (PEC) cells by using various metal oxide photoanodes, such as Fe<sub>2</sub>O<sub>3</sub>, WO<sub>3</sub>, SnO<sub>2</sub>, and BiVO<sub>4</sub> [1–4]. TiO<sub>2</sub> (rutile) is one of the most favorable photoanode materials because it is earth-abundant, inexpensive, nontoxic, applicable in a wide pH range, and highly resistive to photocorrosion [5]. However, the wide band gap of TiO<sub>2</sub> (3.0 eV) limits the photogeneration of charge carriers under visible-light irradiation. Moreover, TiO<sub>2</sub> exhibits low electron mobility (1 cm<sup>2</sup>V<sup>−1</sup>s<sup>−1</sup>) and a short minority carrier (hole) diffusion length (10–100 nm), yielding a low quantum efficiency [6,7]. Accordingly, various approaches have been explored to improve the PEC performance of TiO<sub>2</sub>, including control of the electrode morphology, energy band gap, charge carrier concentration, hetero-nanostructure, and co-catalysts [8–11].

Nanostructured TiO<sub>2</sub> with a large specific surface area has been explored for enhancing the quantum efficiency because the recombination rate of electron–hole pairs can be reduced by reducing the diffusion length of minority carriers to the surface [12,13]. In

particular, one-dimensional (1D) TiO<sub>2</sub> nanostructures, such as nanotubes, nanowires, and nanorods (NRs), have been extensively studied as photoanode materials because they provide an abundant surface area for light absorption and favorable charge transport along the vertical direction [14,15]. However, an inevitable challenge remains in the facile synthesis of highly crystalline 1D nanostructures, because a low crystallinity might induce recombination. From this perspective, hydrothermal reactions are attractive because they can grow highly crystalline and vertically aligned 1D nanostructures with a large surface area at a relatively low temperature [16,17].

The heterojunctions between metal-organic frameworks (MOFs) and oxide semiconductors such as BiVO<sub>4</sub>/MIL-101, ZnO/ZIF-8 and Bi<sub>2</sub>WO<sub>6</sub>/UiO-66 have been recently employed as photocatalysts [18–20] because of the excellent controllability of the light absorption and charge separation by the modification of the coordination chemistry, energy bandgap, organic ligands, and composition of metal clusters. Although they demonstrated the MOF-induced enhancement of photocatalytic effect, the effect of MOF coating on the PEC water splitting of TiO<sub>2</sub> photoanodes has never been investigated. Note that MIL(125)-NH<sub>2</sub> is a good photocatalyst that employs titanium-oxo-clusters coordinated to the organic linkers, i.e., 2-aminoterephthalic acids, which has a theoretical optical band gap of 2.6 eV that enables semiconducting

\* Corresponding author.

E-mail address: [jongheun@korea.ac.kr](mailto:jongheun@korea.ac.kr) (J.-H. Lee).

<https://doi.org/10.1016/j.apcatb.2018.11.057>

Received 12 September 2018; Received in revised form 13 November 2018; Accepted 18 November 2018

Available online 19 November 2018

0926-3373/ © 2018 Elsevier B.V. All rights reserved.

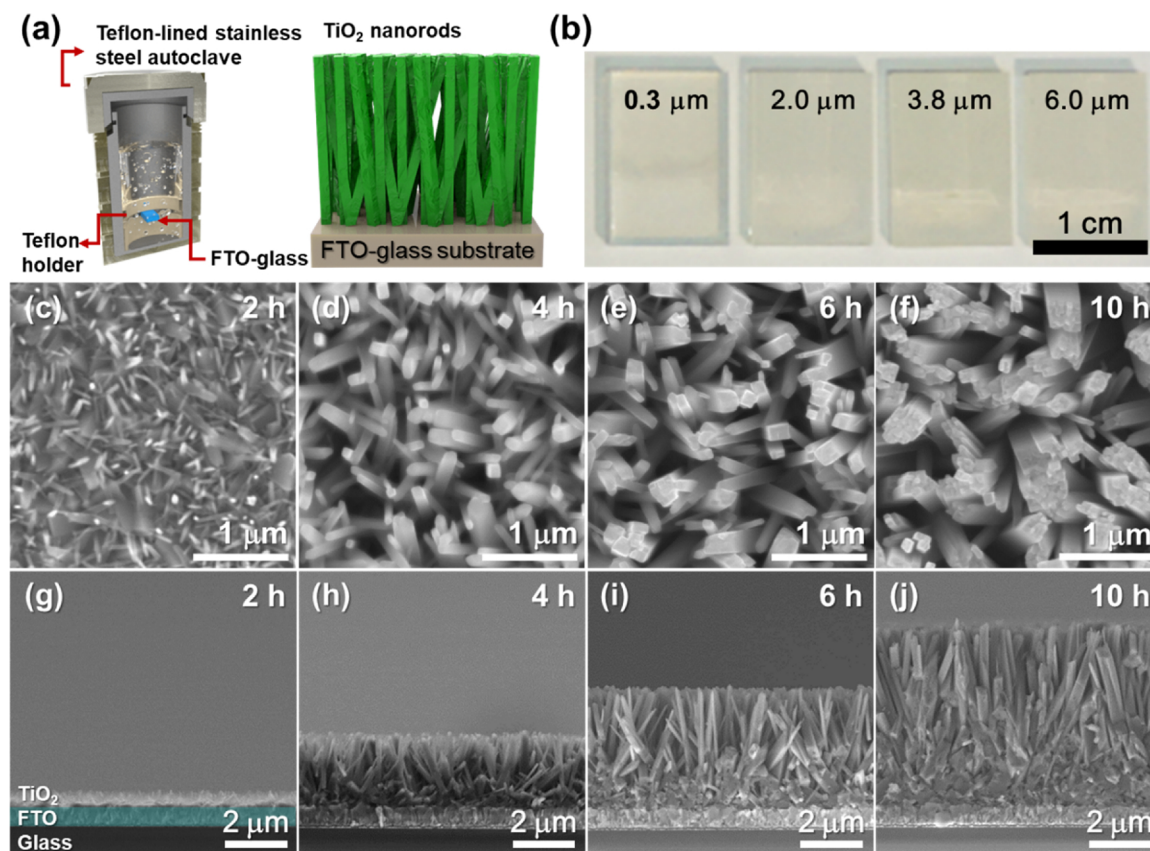


**Fig. 1.** (a) Sketch illustrating our hydrothermal method for growing  $\text{TiO}_2$  NRs on a fluorine-doped tin oxide (FTO)/glass substrate. (b) Photographs of  $\text{TiO}_2$  NRs with different lengths grown on FTO/glass substrates by controlling the hydrothermal growth time (2–10 h). Top-view SEM images of  $\text{TiO}_2$  NRs grown on FTO/glass substrates via a hydrothermal reaction at  $180^\circ\text{C}$  for (c) 2 h, (d) 4 h, (e) 6 h, and (f) 10 h. Cross-sectional SEM images of  $\text{TiO}_2$  NRs grown on FTO/glass substrates via a hydrothermal reaction at  $180^\circ\text{C}$  for (g) 2 h, (h) 4 h, (i) 6 h, and (j) 10 h. The  $\text{TiO}_2$  NRs were annealed at  $600^\circ\text{C}$  for 2 h after the hydrothermal reaction.

application under visible-light [21,22]. Moreover, if the Type (II) band alignment is established at the interface between MIL(125)- $\text{NH}_2$  and  $\text{TiO}_2$  nanostructures, it will facilitate charge separation and electron transfer from the conduction band (CB) of MIL(125)- $\text{NH}_2$  to the CB of  $\text{TiO}_2$  [23,24].

In the present study, we report highly efficient PEC water splitting in  $\text{TiO}_2$  NRs through conformal coating of MIL(125)- $\text{NH}_2$ . Through a facile hydrothermal reaction, strong adhesion between  $\text{TiO}_2$  and MIL(125)- $\text{NH}_2$  can be obtained, yielding a highly stable working performance in an aqueous system. The MIL(125)- $\text{NH}_2/\text{TiO}_2$  NRs exhibited a significantly improved photocurrent density of  $1.63\text{ mA}/\text{cm}^2$  at  $1.23\text{ V}$  vs. a reversible hydrogen electrode (RHE), corresponding to an enhanced incident photon-to-electron conversion efficiency (IPCE) of 84.4% at the maximum absorption wavelength ( $\lambda_{\text{max}} = 340\text{ nm}$ ). The

possible oxidation kinetics underlying the excellent PEC activity were discussed according to the proposed band-bending model.

## 2. Experimental

### 2.1. Preparation of pristine $\text{TiO}_2$ NRs

$\text{TiO}_2$  NRs were grown on an FTO/glass substrate via a hydrothermal reaction. In a typical synthesis process, 0.4-mL of titanium (IV) butoxide (Aldrich Chemicals, 97%) was added to 28-mL of an aqueous HCl solution (the 1:1 (v/v) mixture of deionized (DI) water and 37% HCl) under magnetic stirring to form a clear solution. The solution was transferred to a Teflon-lined stainless-steel autoclave (volume: 100 mL), and the FTO/glass substrate was immersed in the solution. The

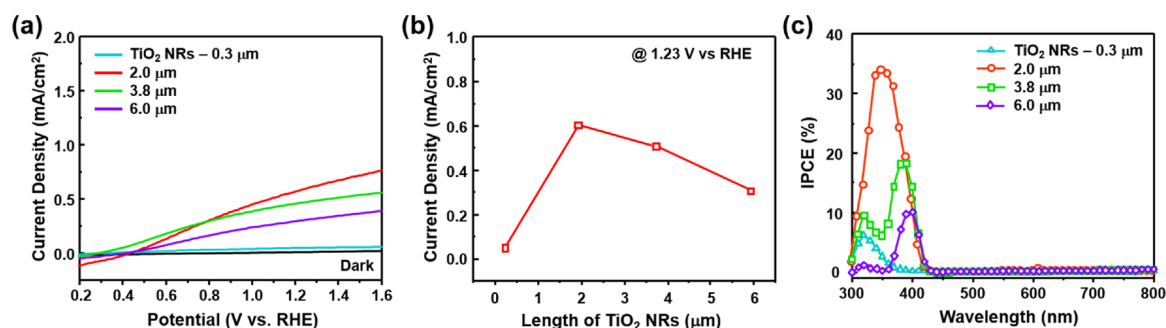


**Fig. 2.** (a) Current density–voltage ( $J$ – $V$ ) curves of  $\text{TiO}_2$  NRs with different lengths in the 1 M NaOH electrolyte, under calibrated 1-sun ( $100\text{ mW}/\text{cm}^2$ ) illumination. (b) Current density of  $\text{TiO}_2$  NRs with lengths of 0.3, 2.0, 3.8, and  $6.0\text{ }\mu\text{m}$  at  $1.23\text{ V}$  vs. RHE. (c) IPCE measurements of  $\text{TiO}_2$  NRs with different lengths at  $1.23\text{ V}$  vs. RHE.

autoclave was sealed and heated to 180 °C for 2, 4, 6, and 10 h. After cooling, the samples were rinsed with DI water a few times. The TiO<sub>2</sub> NRs were annealed at 600 °C for 2 h to remove organic residuals and fully converted into the rutile phase.

## 2.2. Preparation of MIL(125)-NH<sub>2</sub>/TiO<sub>2</sub> NRs

MIL(125)-NH<sub>2</sub> was grown on the TiO<sub>2</sub> NRs via an additional hydrothermal reaction. The 1.5 mmol of 2-aminoterephthalic acid was dissolved in 15-mL dimethylformamide (DMF, Aldrich Chemicals) and 0.5 mmol of titanium butoxide was dissolved in 15-mL methanol. Two solutions are mixed and homogenized by stirring. The mixed solution was kept in a Teflon-lined stainless-steel autoclave, and a TiO<sub>2</sub> NRs/FTO/glass substrate immersed in it. The sealed autoclave was heated to 150 °C for 20 h. The samples were rinsed with DMF and methanol a few times. Note that the organic components within the pores of MIL(125)-NH<sub>2</sub> are known to be exchanged with methanol [25]. Finally, the methanol in the pores of MIL(125)-NH<sub>2</sub> was removed further by heat treatment in vacuum at 80 °C for 2 h.

## 2.3. Materials characterization

Morphological and structural characterizations of the TiO<sub>2</sub> NRs and MIL(125)-NH<sub>2</sub>/TiO<sub>2</sub> NRs were conducted using a field-emission scanning electron microscope (S-4800), by applying an acceleration voltage of 5–10 kV and high-resolution transmission electron microscopy (HR-TEM, Talos F200X, FEI Co., USA). The phase and crystal structure of the TiO<sub>2</sub> NRs and MIL(125)-NH<sub>2</sub>/TiO<sub>2</sub> NRs were investigated via X-ray diffraction (XRD, D/MAX-2500 V/PC, Rigaku, Japan; CuKα, λ = 1.5418 Å). The reflection (R) and transmission (T) of the photoanode were measured using UV–vis spectroscopy (UV–vis, Jasco V-650). The band-bending in the MIL(125)-NH<sub>2</sub>/TiO<sub>2</sub> NRs was investigated using ultraviolet photoemission spectroscopy (UPS, AXIS-Nova; monochromatic He I = 21. eV, Ag 3d5/2 < 0.48 eV), X-ray photoelectron spectroscopy (XPS, AXIS-Nova; monochromatic Al-Kα = 1486.6 eV, Ag 3d5/2 < 100 meV), and UV–vis.

## 2.4. PEC measurements

PEC water splitting was conducted in a 1 M NaOH (pH 13.6) electrolyte using a potentiostat (Ivium Technologies) and a three-electrode electrochemical system equipped with MIL(125)-NH<sub>2</sub>/TiO<sub>2</sub> NRs as the working electrode, a Pt mesh as the counter electrode, and Ag/AgCl/saturated NaCl as the reference electrode. A filter with the standard solar radiation of AM 1.5 G was installed in the solar simulator and was calibrated to 1 sun (100 mW/cm<sup>2</sup>). The photoanodic performance was measured in the dark and under illumination using LSV scanning from the cathodic potential to the anodic potential at a scan rate of 10 mV s<sup>-1</sup>. The measured potential vs. Ag/AgCl was converted to RHE using the Nernst equation [26]:

$$E_{\text{RHE}} = E_{\text{Ag}} + \frac{E_{\text{Ag}}^0}{\text{AgCl}} + 0.059 * \text{pH}, \quad (1)$$

where  $E_{\text{RHE}}$  is the converted potential vs. RHE,  $E_{\text{Ag}/\text{AgCl}}^0 = 0.1976 \text{ V}$ , and  $E_{\text{Ag}/\text{AgCl}}$  is the measured potential vs. RHE and the Ag/AgCl reference. The IPCE was measured at an applied voltage of 1.23 V vs. RHE under the irradiation source and monochromator (MonoRa150). The intensity at each wavelength was measured using a calibrated Si photodiode. The IPCE rate was calculated using the following equation [27]:

$$\text{IPCE (\%)} = \frac{I_{\text{ph}} (\text{mA cm}^{-2}) \times 1239.8 (\text{V nm})}{P_{\text{mono}} (\text{mW cm}^{-2}) \times \lambda (\text{nm})} \times 100 \quad (2)$$

where  $I_{\text{ph}}$  is the measured photocurrent density,  $\lambda$  is the wavelength of the incident light, and  $P_{\text{mono}}$  is the power intensity of the incident light at each wavelength. The IPCE takes three main factors into

consideration: light absorption efficiency ( $\eta_{\text{abs}}$ ), charge separation efficiency ( $\eta_{\text{sep}}$ ), and charge transfer efficiency ( $\eta_{\text{trans}}$ ) [27].

$$\text{IPCE} (\lambda) = \eta_{\text{abs}} \times \eta_{\text{sep}} \times \eta_{\text{trans}} \quad (3)$$

The EIS spectra were measured in a frequency range of 100 kHz to 0.1 Hz with an applied voltage of 1.23 V vs. RHE. The EIS curves were fitted and analyzed to obtain  $R_s$  (series resistance),  $C_{\text{ct}}$  (constant phase element), and  $R_{\text{ct}}$  (charge transfer resistance at the interface between the electrode and the electrolyte). The product of the light-absorption and charge separation efficiencies ( $\eta_{\text{abs}} \times \eta_{\text{sep}}$ ) and  $\eta_{\text{trans}}$  was obtained by adding 1 M Na<sub>2</sub>SO<sub>3</sub> to a 0.5 M buffered phosphate electrolyte (pH = 7) as a fast hole scavenger [28].

## 3. Results and discussion

TiO<sub>2</sub> NRs were hydrothermally grown on an FTO/glass substrate, by modifying a previously reported method [29]. Fig. 1(a) shows a Teflon-lined stainless-steel autoclave containing an FTO/glass substrate inserted in a specially designed Teflon holder, allowing the *in-situ* growth of TiO<sub>2</sub> NRs on the FTO/glass substrate. The hydrothermal reaction is a simple and promising route for growing highly crystalline TiO<sub>2</sub> on an FTO/glass substrate from an aqueous titanium precursor solution at a mild temperature and under a highly pressurized condition. The FTO has a tetragonal rutile structure ( $a = b = 0.4687 \text{ nm}$ ), which reduces the lattice mismatch with rutile TiO<sub>2</sub> ( $a = b = 0.4594 \text{ nm}$ ) to 2% [30,31]. This negligible lattice mismatch is known to offer favorable sites for epitaxial nucleation and the growth of rutile TiO<sub>2</sub> NRs on the FTO/glass substrate [32]. The diameter and length of the NRs were controlled by increasing the hydrothermal growth time from 2 to 10 h. After 2 h of the hydrothermal reaction, it was difficult to observe the differences in transparency with the naked eye. When the hydrothermal reaction time reached 4–10 h, the TiO<sub>2</sub> NRs on the FTO/glass substrate exhibited an opaque and white surface (Fig. 1(b)). Detailed top-view and cross-sectional SEM images of the TiO<sub>2</sub> NRs with respect to the hydrothermal growth time are shown in Fig. 1(c)–(j). The TiO<sub>2</sub> NRs were grown nearly perpendicular to the substrate. The TiO<sub>2</sub> NRs grown for 2, 4, 6, and 10 h were 20, 80, 150, and 300 nm thick (Fig. 1(c)–(f)) and 0.3, 2.0, 3.8, and 6.0 μm long (Fig. 1(g)–(j)), respectively. The XRD patterns of the TiO<sub>2</sub> NRs grown on the FTO/glass substrate are shown in Fig. S1. After annealing at 600 °C, the TiO<sub>2</sub> NRs consisted of a single rutile phase (JCPDS #21-1276), and no anatase phase was detected.

Fig. 2(a) shows the photocurrent densities of TiO<sub>2</sub> NRs with different lengths in a 1 M NaOH electrolyte (pH 13.6). The onset potentials (V vs. RHE) in linear sweep voltammetry (LSV) were all close to ~0.4 V. The photocurrent densities (1.23 V vs. RHE) are plotted with respect to the NR length in Fig. 2(b). The 0.3-μm-long TiO<sub>2</sub> NRs showed negligible photocurrent density of 0.05 mA/cm<sup>2</sup> at 1.23 V vs. RHE, probably because their limited surface area did not provide sufficient active sites for light absorption and PEC activity. Significant enhancement of the photocurrent density (0.6 mA/cm<sup>2</sup> at 1.23 V vs. RHE) was achieved when the TiO<sub>2</sub> NRs were hydrothermally grown to a length of 2 μm. However, the photocurrent density decreased to 0.51 (3.8 μm) and 0.31 (6.0 μm) mA/cm<sup>2</sup> at 1.23 V vs. RHE with the further growth of the NRs. The TiO<sub>2</sub> NRs with a length of 2 μm exhibited the highest IPCE (1.23 V vs. RHE) of 33.9% at λ = 350 nm and a significant decline between λ = 380 nm and λ = 420 nm (Fig. 2(c)). This is consistent with the reported results that rutile TiO<sub>2</sub> shows an abrupt decrease in absorption in the wavelength range of 380–420 nm [33,34]. For TiO<sub>2</sub> NRs, wavelengths shorter than 380 nm are known to be mainly absorbed at the top part of the NRs [35]. Hence, lower IPCE would be yielded below 380 nm, as the photoinduced electrons had to pass through the entire length of the NRs to reach the FTO. The 0.3-μm-long TiO<sub>2</sub> NRs, which are expected to provide a short travel length to FTO for photoinduced electrons but an insufficient surface area for efficient photon absorbance, exhibited maximum IPCE at 320 nm. This implies



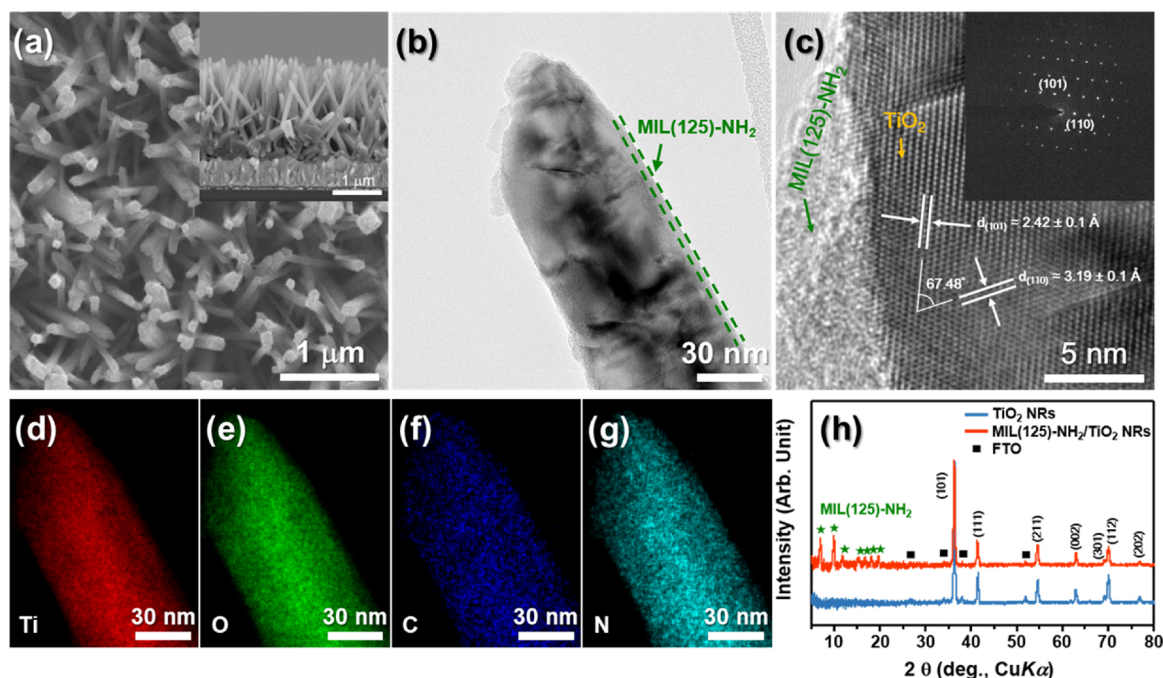


**Fig. 3.** (a) Top-view SEM image of MIL(125)-NH<sub>2</sub>/TiO<sub>2</sub> NRs. Inset: cross-sectional SEM image of MIL(125)-NH<sub>2</sub>/TiO<sub>2</sub> NRs. (b) TEM image of MIL(125)-NH<sub>2</sub>/TiO<sub>2</sub> NRs. (c) High-resolution TEM image with indexing. Inset: selected-area electron diffraction (SAED) pattern of MIL(125)-NH<sub>2</sub>/TiO<sub>2</sub> NRs with indexing. EDS element maps of (d) Ti, (e) O, (f) C, and (g) N. (h) Glancing-angle XRD patterns of hydrothermally grown TiO<sub>2</sub> NRs and the MIL(125)-NH<sub>2</sub>/TiO<sub>2</sub> NR heterojunction on an FTO/glass substrate.

that  $\eta_{sep}$  and  $\eta_{trans}$  are dominant over  $\eta_{abs}$ . On the other hand, when the NR length is increased to 2  $\mu\text{m}$ , the wavelength of the maximum IPCE ( $\lambda_{max}$ ) shifted to 350 nm, showing good agreement with the highest photocurrent density. This demonstrates that 2- $\mu\text{m}$ -long TiO<sub>2</sub> NRs are optimal for yielding high  $\eta_{abs}$ ,  $\eta_{sep}$ , and  $\eta_{trans}$  values simultaneously. However, when the NRs were elongated to 3.8 and 6  $\mu\text{m}$ ,  $\lambda_{max}$  shifted to 390 and 400 nm, respectively, with a degraded IPCE value. The reduction of the IPCE indicates that the path for the charge carriers to reach the FTO back contact was too long, and the shift of  $\lambda_{max}$  to the longer wavelength indicates that  $\eta_{abs}$  was dominant over  $\eta_{sep}$  and  $\eta_{trans}$ . This is in agreement with the literature results, in which rutile TiO<sub>2</sub> exhibited a shift to a higher  $\lambda_{max}$  of the IPCE for longer NRs [35].

The heterojunction can be established to enhance the PEC performance by increasing the lifetime of separated charge carriers in TiO<sub>2</sub> NRs. For this, we designed an MIL(125)-NH<sub>2</sub>/TiO<sub>2</sub> NR heterojunction photoanode via a hydrothermal reaction. In a typical synthesis of MIL(125)-NH<sub>2</sub>/TiO<sub>2</sub> NRs, titanium butoxide and 2-aminoterephthalic acid are dissolved in the solution containing TiO<sub>2</sub> NRs. The nucleation and growth starts to form the framework with Ti<sub>8</sub>O<sub>8</sub>(OH)<sub>4</sub>-(O<sub>2</sub>CC<sub>6</sub>H<sub>5</sub>-CO<sub>2</sub>-NH<sub>2</sub>)<sub>6</sub> as a basic building unit having a bipyrmaid structure with six cyclic octamers of Ti<sub>8</sub>O<sub>20</sub>(OH)<sub>4</sub> at the corner bonded by eight NH<sub>2</sub>-BDC linkers (Fig. S2) [36]. The OH groups in NH<sub>2</sub>-BDC linkers will facilitate the bonding with TiO<sub>2</sub> NRs. The hydrothermal synthesis offers well-attached, conformal, large-area, and uniform growth of MIL(125)-NH<sub>2</sub> on the entire surface of the TiO<sub>2</sub> NRs. This is desirable in PEC activities, as strong bonding between TiO<sub>2</sub> and MIL(125)-NH<sub>2</sub> provides a stable working performance in an aqueous system for charge carrier collection and transportation. MIL(125)-NH<sub>2</sub> is an MOF composed of titanium oxo-clusters coordinated to 2-aminoterephthalic acid as an organic ligand in its crystal structure (Fig. S3). MIL(125)-NH<sub>2</sub> is known to exhibit a semiconducting property with a band gap energy of  $\sim 2.6$  eV [21,22]. The semiconducting characteristics, as well as the versatile modification of metal ions and organic linkers of MIL(125)-NH<sub>2</sub>, facilitate the amelioration of the PEC activity of TiO<sub>2</sub> NRs. When MIL(125)-NH<sub>2</sub> is used as a photocatalyst, photoinduced electrons excited to the titanium-oxo-clusters (LUMO) reduce Ti<sup>4+</sup> to Ti<sup>3+</sup>. Accordingly, holes are left

behind at the organic linkers (HOMO) and expected to be consumed for water oxidation in PEC water splitting. Such a facilitated transfer of photogenerated electrons is achieved by a prompt ligand-to-metal charge transfer (LMCT) [37,38]. The color of the substrate changed from white to yellow after the hydrothermal growth of MIL(125)-NH<sub>2</sub> on the TiO<sub>2</sub> NRs (Fig. S4). MIL(125)-NH<sub>2</sub> was uniformly coated on the surface of TiO<sub>2</sub> NRs without any structural distortion (Fig. 3(a) and (b)). Close examination via HR-TEM (Fig. 3(b) and (c)) confirmed that a very thin MIL(125)-NH<sub>2</sub> layer (thickness: 5–10 nm) was coated on the surface of TiO<sub>2</sub> NRs and revealed that the TiO<sub>2</sub> NRs consist of a single-crystalline structure, according to the analysis of the SAED patterns. The inter-planar spacing in the lattice fringes were analyzed to be  $d_{(101)} = 2.42 \pm 0.1$  Å and  $d_{(110)} = 3.19 \pm 0.1$  Å, corresponding to the rutile phase of TiO<sub>2</sub> [39,40]. Elemental mapping (Fig. 3(d)–(g)) suggested that the MIL(125)-NH<sub>2</sub> layer was coated on the entire surface of the TiO<sub>2</sub> NRs in a uniform manner. Most of the XRD peaks in the range of  $2\theta = 5$ – $25^\circ$  were assigned to MIL(125)-NH<sub>2</sub> (Fig. 3(h)) and were consistent with simulated patterns of MIL(125)-NH<sub>2</sub> (Fig. S5) [41]. The fine-scan XPS spectra for Ti 2p<sub>1/2</sub> and Ti 2p<sub>3/2</sub> are shown in (Fig. S6). The Ti 2p<sub>3/2</sub> spectrum of pristine TiO<sub>2</sub> NRs consists of two contributions from Ti<sup>4+</sup> (458.1 eV) and Ti<sup>3+</sup> (457.7 eV) for TiO<sub>2</sub> (Fig. S6(a)) [42], leading to the entire Ti 2p<sub>3/2</sub> spectrum peaked at 458.0 eV. In contrast, Ti 2p<sub>3/2</sub> spectrum in MIL(125)-NH<sub>2</sub> shows the maximum intensity at the higher binding energy (458.8 eV), which is attributed to Ti<sup>4+</sup> in MIL(125)-NH<sub>2</sub> (Fig. S6(c)) [41,43]. Note that the peak position (458.2 eV) of Ti 2p<sub>3/2</sub> spectrum in MIL(125)-NH<sub>2</sub>/TiO<sub>2</sub> NRs is located between above two peaks. This supports again the coexistence of MIL(125)-NH<sub>2</sub> and TiO<sub>2</sub> NRs. The increase of the amount of 2-aminoterephthalic acid from 0.5 to 3.0 mmol in the precursor solutions promoted the formation of MIL(125)-NH<sub>2</sub> on the TiO<sub>2</sub> NRs (Fig. S7). No remarkable structural changes were observed when 0.5 mmol of 2-aminoterephthalic acid were employed for the hydrothermal reaction (Fig. S7(a)). When the amount of 2-aminoterephthalic acid was increased to 3.0 mmol, the MIL(125)-NH<sub>2</sub> covered almost the whole area in an irregular manner (Fig. S7(d)). Fig. S8 shows the photocurrent densities of the TiO<sub>2</sub> NRs at 1.23 V vs. RHE with different amounts of MIL(125)-NH<sub>2</sub> coated on the

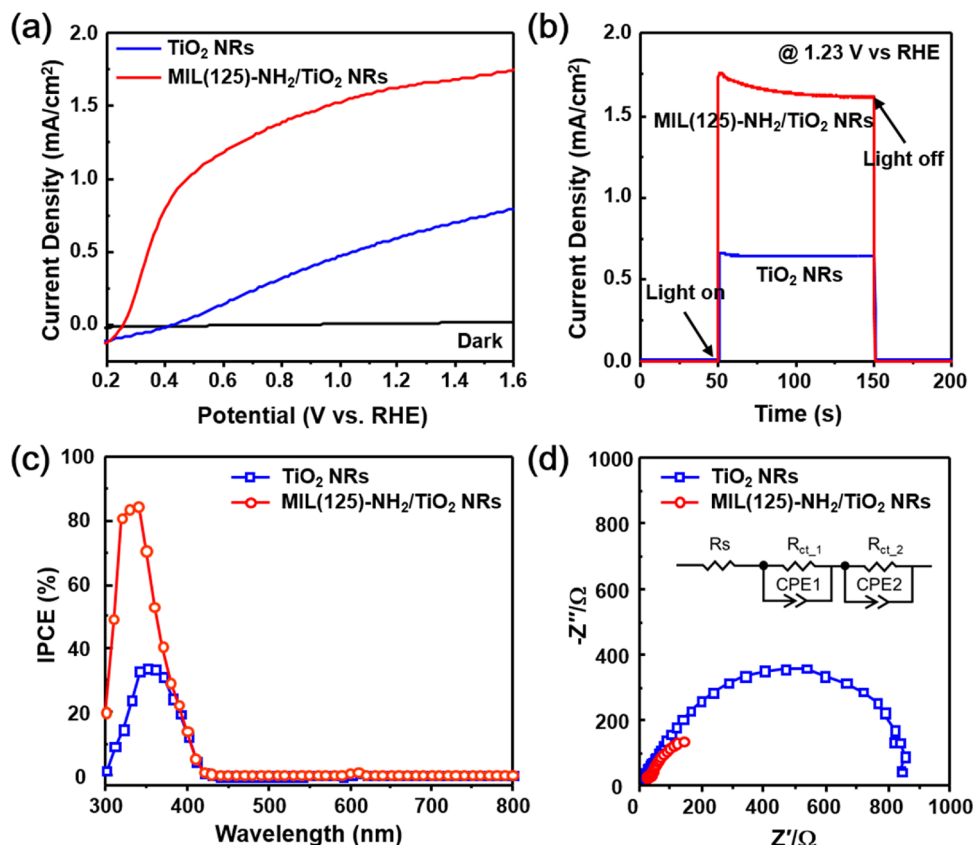


**Fig. 4.** (a)  $J$ - $V$  curves of  $\text{TiO}_2$  NRs and  $\text{MIL}(125)\text{-NH}_2/\text{TiO}_2$  NRs in a 1 M NaOH electrolyte. (b) Comparison of the photocurrent density between  $\text{TiO}_2$  NRs and  $\text{MIL}(125)\text{-NH}_2/\text{TiO}_2$  NRs at 1.23 V vs. RHE. (c) IPCE measurements of  $\text{TiO}_2$  NRs and  $\text{MIL}(125)\text{-NH}_2/\text{TiO}_2$  NRs. (d) EIS analysis of  $\text{TiO}_2$  NRs and  $\text{MIL}(125)\text{-NH}_2\text{-TiO}_2$  NRs.

**Table 1**

Fitted charge transfer resistance.

Photoanode	$R_s$ ( $\Omega \text{ cm}^2$ )	$R_{ct,1}$ ( $\Omega \text{ cm}^2$ )	$R_{ct,2}$ ( $\Omega \text{ cm}^2$ )
$\text{TiO}_2$ NRs	3.53	20.20	853.98
$\text{MIL}(125)\text{-NH}_2/\text{TiO}_2$ NRs	4.75	14.18	301.71

surface. The photocurrent density improved with the increase of the amount of  $\text{MIL}(125)\text{-NH}_2$  coated on the  $\text{TiO}_2$  NRs but deteriorated significantly when 3.0 mmol of 2-aminoterephthalic acid was employed. Accordingly, 1.5 mmol 2-aminoterephthalic acid-assisted  $\text{MIL}(125)\text{-NH}_2$  growth on the  $\text{TiO}_2$  NRs exhibited the highest PEC activity at 1.23 V vs. RHE.

Fig. 4(a) shows the photocurrent densities of pristine  $\text{TiO}_2$  NRs and  $\text{MIL}(125)\text{-NH}_2/\text{TiO}_2$  NRs in a 1 M NaOH electrolyte. Compared with pristine  $\text{TiO}_2$  NRs,  $\text{MIL}(125)\text{-NH}_2/\text{TiO}_2$  NRs exhibited a remarkably high PEC performance of  $1.63 \text{ mA}/\text{cm}^2$  at 1.23 V vs. RHE. This represents unprecedentedly high catalytic performance for PEC activity of  $\text{TiO}_2$ -based photoanodes (Table S1). In addition, we observed that the onset potential (V vs. RHE) in LSV shifted down from 0.44 to 0.27 V when  $\text{MIL}(125)\text{-NH}_2$  was coated on the  $\text{TiO}_2$  NRs. According to the redox potential data for  $\text{MIL}(125)\text{-NH}_2$  and  $\text{TiO}_2$ , the facilitated water oxidation kinetics can be attributed to the efficient light absorption and charge transfer, which led to a lower potential to promote water splitting [44,45]. To confirm the effect of  $\text{MIL}(125)\text{-NH}_2$  on the PEC activity, it was also coated on a commercial  $\text{TiO}_2$  (Degussa P25) film printed on an FTO/glass substrate via the doctor blade method. The photocurrent density of  $\text{MIL}(125)\text{-NH}_2/\text{P25}$  was almost twice as high as that of P25 at 1.23 V vs. RHE, as shown in Fig. S9, confirming that the coating of  $\text{MIL}(125)\text{-NH}_2$  on the  $\text{TiO}_2$  photoanode is a promising

approach for enhancing the PEC properties. The light on/off transient curves of the  $\text{TiO}_2$  NRs and  $\text{MIL}(125)\text{-NH}_2/\text{TiO}_2$  NRs were analyzed by measuring the amperometric photocurrent by applying a steady potential of 1.23 V (V vs. RHE) in the dark and under illumination (Fig. 4(b)). Both photoanodes showed steep inclination of the photocurrent under initial illumination, followed by a relaxed steady state. To understand the effect of  $\text{MIL}(125)\text{-NH}_2$  on  $\text{TiO}_2$  NRs, the IPCE spectra were measured from 300 to 800 nm at an applied potential of 1.23 V vs. RHE (Fig. 4(c)).  $\text{MIL}(125)\text{-NH}_2/\text{TiO}_2$  NRs exhibited the highest IPCE of 84.4% at  $\lambda = 340 \text{ nm}$ , which is almost 2.5 times higher than that of pristine  $\text{TiO}_2$  NRs. The IPCE decreased nearly to zero when the incident wavelengths became longer than 430 nm. The IPCE enhancement in the  $\lambda = 300\text{--}350\text{-nm}$  region could be assigned to the active reduction of  $\text{Ti}^{4+}$  to  $\text{Ti}^{3+}$  in  $\text{MIL}(125)\text{-NH}_2$ , followed by the transportation of electrons from  $\text{Ti}^{3+}$  to  $\text{TiO}_2$ , which prolonged the lifetime of separated charge carriers [44,46]. The electrochemical impedance spectroscopy (EIS) spectra of pristine  $\text{TiO}_2$  NRs and  $\text{MIL}(125)\text{-NH}_2/\text{TiO}_2$  NRs were measured to analyze the charge carrier transport at an applied potential of 1.23 V vs. RHE (Fig. 4(d)). An equivalent circuit for the EIS spectra is shown in the inset of Fig. 4(d). The obtained results shown in the Nyquist plots were fitted and calculated to determine the exact value of the resistance at the interfaces, as shown in Table 1. The  $R_{ct}$  values (charge transfer resistances at the interface between the electrode and the electrolyte) for the  $\text{MIL}(125)\text{-NH}_2/\text{TiO}_2$  NRs were lower than those for the  $\text{TiO}_2$  NRs, indicating that the charge transfer was facilitated efficiently through the interface of  $\text{TiO}_2$  NRs and the electrolyte by  $\text{MIL}(125)\text{-NH}_2$  coating, which then enhanced the corresponding PEC activity. Aside from charge transfer properties, light absorption and charge separation efficiencies are another critical factors that need to be studied in the aspect of PEC performance. Light harvesting efficiency (LHE) is calculated (see Fig. S10) and plotted in Fig. 5(a); strong light absorptions were observed in  $\lambda = 300\text{--}412 \text{ nm}$  for  $\text{TiO}_2$  NRs and  $\lambda = 300\text{--}415 \text{ nm}$

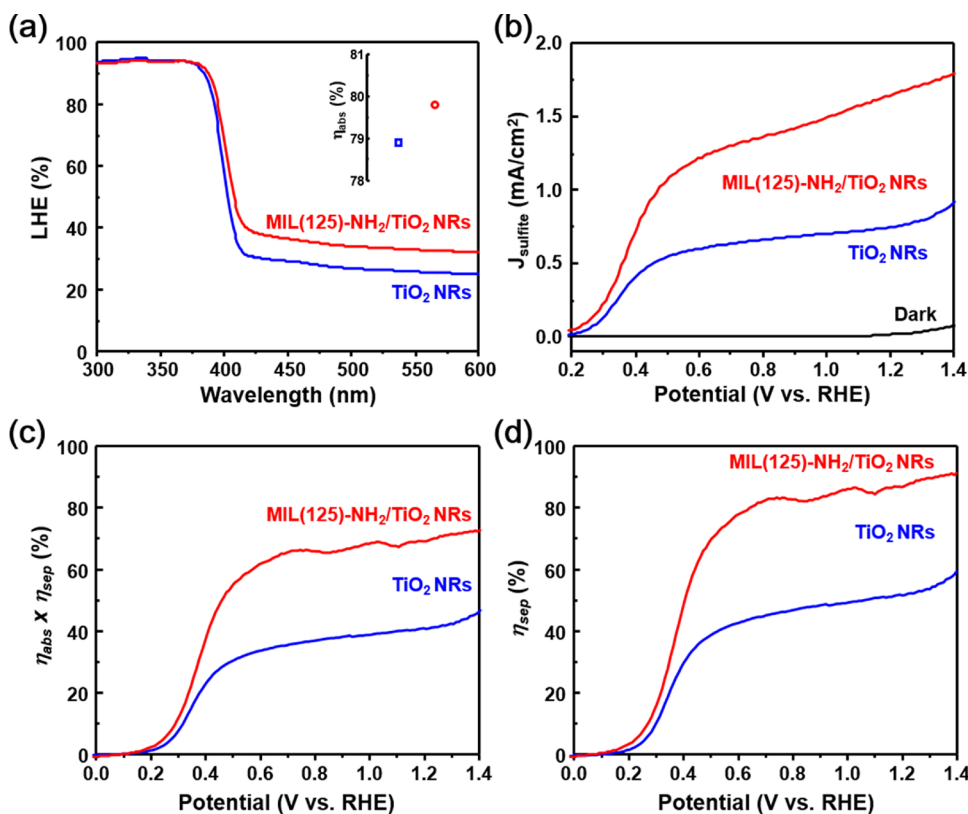


**Fig. 5.** (a) LHE (%) of TiO<sub>2</sub> NRs and MIL(125)-NH<sub>2</sub>/TiO<sub>2</sub> NRs. Inset: integrated light-absorption efficiency ( $\eta_{abs}$ ). (b)  $J$ - $V$  curves under simulated AM 1.5 G illumination with 1 M Na<sub>2</sub>SO<sub>3</sub> added to the 0.5 M buffered phosphate electrolyte (pH = 7) as a hole scavenger. (c) Product of light absorption and charge separation efficiency ( $\eta_{abs} \times \eta_{sep}$ ) vs. potential, with the dark currents subtracted. (d) Charge separation efficiency ( $\eta_{sep}$ ) with dark current subtracted.

for MIL(125)-NH<sub>2</sub>/TiO<sub>2</sub> NRs. The transmittance and the reflectance in Fig. S10 showed a little difference, suggesting the light absorbance was not significantly affected by MIL(125)-NH<sub>2</sub> coating. By integrating the absorbance across AM 1.5 G solar spectrum, the estimated  $\eta_{abs}$  value of pristine TiO<sub>2</sub> NRs and MIL(125)-NH<sub>2</sub>/TiO<sub>2</sub> NRs were 78.9% and 79.8% (see Fig. 5(a) inset and Fig. S11). Although MIL(125)-NH<sub>2</sub>/TiO<sub>2</sub> NRs yielded higher  $\eta_{abs}$  than the pristine TiO<sub>2</sub> NRs it was not sufficient enough to explain nearly 3 times higher photocurrent of the MIL(125)-NH<sub>2</sub>/TiO<sub>2</sub> NRs. Therefore we examined the charge separation efficiency in relation to the water photooxidation current density expressed in Equation 4 [28,47,48].

$$J_{H_2O} = J_{max} \times \eta_{abs} \times \eta_{sep} \times \eta_{trans} \quad (4)$$

First, to measure the  $\eta_{abs} \times \eta_{sep}$  product in Equation 4, 1 M Na<sub>2</sub>SO<sub>3</sub> was introduced to the 0.5 M phosphate buffered electrolyte (pH = 7) as a hole scavenger to induce nearly 100% of  $\eta_{trans}$  (Fig. 5(b)), at this moment sulfite oxidation photocurrent density is given by  $J_{sulfite} \approx J_{max} \times \eta_{abs} \times \eta_{sep}$  [49]. Here we can assume  $\eta_{abs} \times \eta_{sep} \approx J_{sulfite}/J_{max}$ . Pristine TiO<sub>2</sub> NRs and MIL(125)-NH<sub>2</sub>/TiO<sub>2</sub> NRs exhibit  $J_{sulfite}$  values of 0.76 mA/cm<sup>2</sup> and 1.74 mA/cm<sup>2</sup> at 1.23 V vs. RHE, respectively, which correspond to a smaller  $\eta_{abs} \times \eta_{sep}$  product of TiO<sub>2</sub> NRs (41.1%) than that of MIL(125)-NH<sub>2</sub>/TiO<sub>2</sub> NRs (69.9%) with the dark current subtracted (Fig. 5(c)). Moreover, the charge separation efficiencies are plotted in Fig. 5(d);  $\eta_{sep}$  for pristine TiO<sub>2</sub> NRs and MIL(125)-NH<sub>2</sub>/TiO<sub>2</sub> NRs at 1.23 V vs. RHE were 52.1% and 87.6% respectively. Considering the charges generated from the ~10 nm thick MIL(125)-NH<sub>2</sub> coating on the TiO<sub>2</sub> NRs surface, holes can easily reach the semiconductor/electrolyte interface and participate in water oxidation kinetics as the distance they need to travel is shorter than the reported hole diffusion length [6,7]. This indicates the charge recombination rate is decreased by the conformal coating of MIL(125)-NH<sub>2</sub> on TiO<sub>2</sub> NRs.

In addition, to understand the dynamics of light absorption, charge separation, and surface charge transfer, the band-bending in the MIL(125)-NH<sub>2</sub>/TiO<sub>2</sub> NRs was investigated using UPS, XPS, and UV-vis

spectroscopy. Fig. 6(a) shows the secondary-electron emission (SEE) spectra of TiO<sub>2</sub> NRs, MIL(125)-NH<sub>2</sub>, and reference Au foil electrodes. The work functions of TiO<sub>2</sub> and MIL(125)-NH<sub>2</sub> are determined to be 4.02 and 3.12 eV from the SEE cutoffs respectively, while that of the Au reference is 5.1 eV. The XPS results (Fig. 6(b)) revealed the energy difference between the Fermi level and the valence-band maximum ( $E_F - E_v$ ) of TiO<sub>2</sub> NRs to be 2.80 eV and that of MIL(125)-NH<sub>2</sub> to be 2.20 eV. The energy band gap values of TiO<sub>2</sub> NRs and MIL(125)-NH<sub>2</sub> were calculated to be 2.98 and 2.6 eV, respectively, according to the UV-vis spectra (Fig. 6(c)), which agrees with the values in the previous works [5,22]. A schematic energy band diagram for MIL(125)/TiO<sub>2</sub> NRs is shown in Fig. 6(d), indicating a Type (II) junction in an equilibrium state [44,46]. Under UV-vis illumination, the photoinduced electrons from the organic linker are transferred to the titanium-oxo clusters (LMCT), reducing Ti<sup>4+</sup> into Ti<sup>3+</sup> and leaving the holes behind [50]. As the CB ( $E_c$ ) of TiO<sub>2</sub> NRs (3.84 eV vs. vacuum) is more negative than that of MIL(125)-NH<sub>2</sub> (3.62 eV vs. vacuum) electrons in MIL(125)-NH<sub>2</sub> are favorable for transport to the interface of TiO<sub>2</sub> NRs, while holes at the  $E_v$  of TiO<sub>2</sub> NRs migrate to the  $E_v$  of MIL(125)-NH<sub>2</sub>. Thus, the photoinduced electron-hole pairs can be separated efficiently in the MIL(125)/TiO<sub>2</sub> NRs, leading to a remarkably enhanced PEC activity. The PEC stability of MIL(125)-NH<sub>2</sub>/TiO<sub>2</sub> NRs at 1.23 V vs. RHE was examined for 10,000 s under simulated AM 1.5 G solar illumination at 100 mW/cm<sup>2</sup> (Fig. 7(a)). Furthermore, the long-term stability of MIL(125)-NH<sub>2</sub>/TiO<sub>2</sub> NRs was evaluated for 1 month under an applied voltage of 1.23 V vs. RHE (Fig. 7(b)). During the measurement, the MIL(125)-NH<sub>2</sub>/TiO<sub>2</sub> NRs exhibited no degradation; and the SEM images (Fig. S12) suggest that the MIL(125)-NH<sub>2</sub> remained on the surface of TiO<sub>2</sub> NRs even after 1-month evaluation. Furthermore, the fine-scan XPS spectrum for MIL(125)-NH<sub>2</sub>/TiO<sub>2</sub> NRs after the 1-month evaluation is compared with the fresh MIL(125)-NH<sub>2</sub>/TiO<sub>2</sub> NRs in Fig. S13. The Ti 2p peak positions in XPS spectra remained similar even after 1-month test, suggesting that the structure of MIL(125)-NH<sub>2</sub> maintained at the surface of TiO<sub>2</sub>. These results indicate that MIL(125)-NH<sub>2</sub>/TiO<sub>2</sub> NRs is electrochemically stable over the long term.

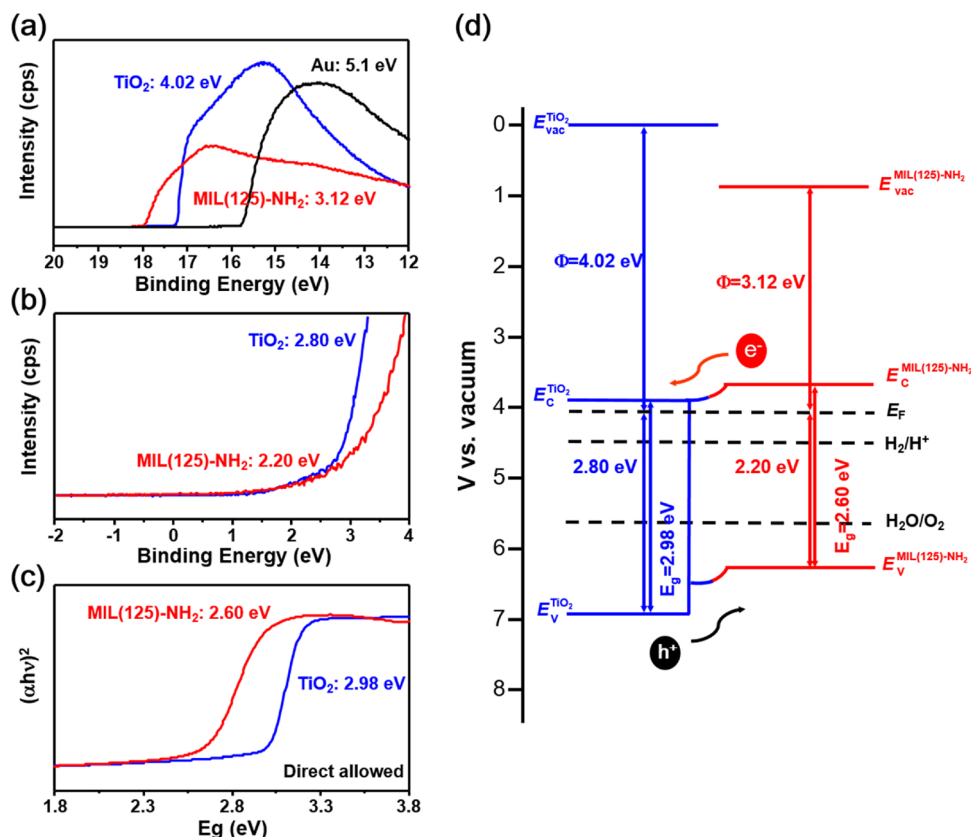


**Fig. 6.** (a) UPS spectra of  $\text{TiO}_2$  NRs, MIL(125)- $\text{NH}_2$ , and reference Au foil. (b) XPS spectra of  $\text{TiO}_2$  NRs and MIL(125)- $\text{NH}_2$ . (c) UV-vis spectra of  $\text{TiO}_2$  NRs and MIL(125)- $\text{NH}_2$ . (d) Schematic energy band diagram of the MIL(125)- $\text{NH}_2/\text{TiO}_2$  NR heterojunction photoanode.

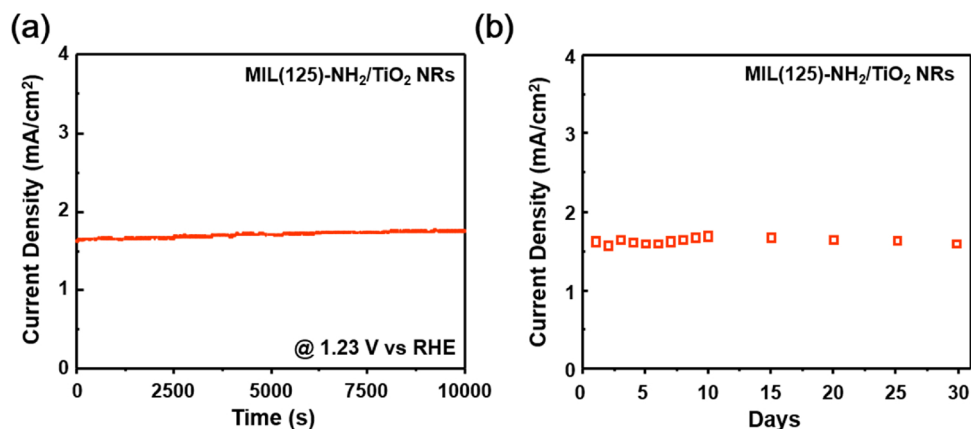


**Fig. 7.** (a) The chronopotentiometry curve of MIL(125)- $\text{NH}_2/\text{TiO}_2$  NRs in a 1 M NaOH electrolyte at 1.23 V vs. RHE with illuminated sunlight. (b) Long-term stability measurement of MIL(125)- $\text{NH}_2/\text{TiO}_2$  NRs for 1 month.

#### 4. Conclusion

MIL(125)- $\text{NH}_2$  coated  $\text{TiO}_2$  NRs were prepared via a two-step hydrothermal reaction and used as a photoanode for PEC water splitting. Compared with pristine  $\text{TiO}_2$  NRs, the MIL(125)- $\text{NH}_2/\text{TiO}_2$  NR heterojunction exhibited a remarkably enhanced photocurrent density of 1.63 mA/cm<sup>2</sup> at 1.23 V vs. RHE without any co-catalyst. We attribute the increase of the PEC activity to the i) effective light absorption and charge transport due to the large surface area and crystallinity of  $\text{TiO}_2$  NRs; ii) the moderate band gap (2.6 eV) of the semiconducting MIL(125)- $\text{NH}_2$ ; iii) the uniform and conformal coating of MIL(125)- $\text{NH}_2$  on the  $\text{TiO}_2$  NRs; and iv) the efficient charge carrier separation and transportation through the type (II) band gap alignment of  $\text{TiO}_2$  and

MIL(125)- $\text{NH}_2$ . PEC using an MIL(125)- $\text{NH}_2/\text{TiO}_2$  NR heterojunction demonstrated excellent stability and recycling performance. This work not only sheds light on the intrinsic effect of the MOF on enhancing the PEC activity through the construction of MOF/semiconductor heterostructures but also introduces a new strategy to design highly efficient MOF-based PEC cells.

#### Acknowledgements

This work was supported by a grant from the National Research Foundation of Korea (NRF), which was funded by the Korean government (Ministry of Education, Science, and Technology (MEST), Grant No. 2016R1A2A1A05005331).



## Appendix A. Supplementary data

Supplementary material related to this article can be found, in the online version, at doi:<https://doi.org/10.1016/j.apcatb.2018.11.057>.

## References

- [1] K. Sivula, F. Le Formal, M. Gratzel, Solar water splitting: progress using hematite ( $\alpha\text{-Fe}_2\text{O}_3$ ) photoelectrodes, *ChemSusChem* 4 (2011) 432–449.
- [2] Y. Pihosh, I. Turkevych, K. Mawatari, T. Asai, T. Hisatomi, J. Uemura, M. Tosa, K. Shimamura, J. Kubota, K. Domen, T. Kitamori, Nanostructured  $\text{WO}_3/\text{BiVO}_4$  photoanodes for efficient photoelectrochemical water splitting, *Small* 10 (2014) 3692–3699.
- [3] S. Abanades, P. Charvin, F. Lemont, G. Flamant, Novel two-step  $\text{SnO}_2/\text{SnO}$  water-splitting cycle for solar thermochemical production of hydrogen, *Int. J. Hydrogen Energy* 33 (2008) 6021–6030.
- [4] T.W. Kim, K.-S. Choi, Nanoporous  $\text{BiVO}_4$  photoanodes with dual-layer oxygen evolution catalysts for solar water splitting, *Science* 343 (2014) 990–994.
- [5] A.L. Linsebigler, G.Q. Lu, J.T. Yates, Photocatalysis on  $\text{TiO}_2$  surfaces - principles, mechanisms, and selected results, *Chem. Rev.* 95 (1995) 735–758.
- [6] E. Hendry, M. Koeberg, B. O'Regan, M. Bonn, Local field effects on electron transport in nanostructured  $\text{TiO}_2$  revealed by terahertz spectroscopy, *Nano Lett.* 6 (2006) 755–759.
- [7] P. Salvador, Hole diffusion length in  $\text{TiO}_2$  single crystals and sintered electrodes: photoelectrochemical determination and comparative analysis, *J. Appl. Phys.* 55 (1984) 2977–2985.
- [8] J.H. Park, S. Kim, A.J. Bard, Novel carbon-doped  $\text{TiO}_2$  nanotube arrays with high aspect ratios for efficient solar water splitting, *Nano Lett.* 6 (2006) 24–28.
- [9] J. Tang, J.R. Durrant, D.R. Klug, Mechanism of photocatalytic water splitting in  $\text{TiO}_2$ . Reaction of water with photoholes, importance of charge carrier dynamics, and evidence for four-hole chemistry, *J. Am. Chem. Soc.* 130 (2008) 13885–13891.
- [10] M.Z. Xie, X.D. Fu, L.Q. Jing, P. Luan, Y.J. Feng, H.G. Fu, Long-lived, visible-light-excited charge carriers of  $\text{TiO}_2/\text{BiVO}_4$  nanocomposites and their unexpected photoactivity for water splitting, *Adv. Energy Mater.* 4 (2014).
- [11] J. Yu, L. Qi, M. Jaroniec, Hydrogen production by photocatalytic water splitting over  $\text{Pt}/\text{TiO}_2$  nanosheets with exposed (001) facets, *J. Phys. Chem. C* 114 (2010) 13118–13125.
- [12] S.C. Warren, K. Voitchovsky, H. Dotan, C.M. Leroy, M. Cornuz, F. Stellacci, C. Hebert, A. Rothschild, M. Gratzel, Identifying champion nanostructures for solar water-splitting, *Nat. Mater.* 12 (2013) 842–849.
- [13] J.F. Zhu, M. Zach, Nanostructured materials for photocatalytic hydrogen production, *Curr. Opin. Colloid Interface Sci.* 14 (2009) 260–269.
- [14] M.G. Walter, E.L. Warren, J.R. McKone, S.W. Boettcher, Q.X. Mi, E.A. Santori, N.S. Lewis, Solar water splitting cells, *Chem. Rev.* 111 (2011) 5815–5815.
- [15] M.Z. Liu, N.D. Snapp, H. Park, Water photolysis with a cross-linked titanium dioxide nanowire anode, *Chem. Sci.* 2 (2011) 80–87.
- [16] M. Ge, Q. Li, C. Cao, J. Huang, S. Li, S. Zhang, Z. Chen, K. Zhang, S.S. Al-Deyab, Y. Lai, One-dimensional  $\text{TiO}_2$  nanotube photocatalysts for solar water splitting, *Adv. Sci. (Weinh.)* 4 (2017) 1600152.
- [17] A. Wolcott, W.A. Smith, T.R. Kuykendall, Y.P. Zhao, J.Z. Zhang, Photoelectrochemical water splitting using dense and aligned  $\text{TiO}_2$  nanorod arrays, *Small* 5 (2009) 104–111.
- [18] Y.L. Xu, M.M. Lv, H.B. Yang, Q. Chen, X.T. Liu, F.Y. Wei,  $\text{BiVO}_4/\text{MIL}-101$  composite having the synergistically enhanced visible light photocatalytic activity, *RSC Adv.* 5 (2015) 43473–43479.
- [19] W.W. Zhan, Q. Kuang, J.Z. Zhou, X.J. Kong, Z.X. Xie, L.S. Zheng, Semiconductor@metal-organic framework core-shell heterostructures: a case of  $\text{ZnO}/\text{ZIF}-8$  nanorods with selective photoelectrochemical response, *J. Am. Chem. Soc.* 135 (2013) 1926–1933.
- [20] Z. Sha, J. Sun, H.S. On Chan, S. Jaenicke, J. Wu, Bismuth tungstate incorporated zirconium metal-organic framework composite with enhanced visible-light photocatalytic performance, *RSC Adv.* 4 (2014) 64977–64984.
- [21] M. de Miguel, F. Ragon, T. Devic, C. Serre, P. Horcajada, H. Garcia, Evidence of photoinduced charge separation in the metal-organic framework  $\text{MIL}-125(\text{Ti})\text{-NH}_2$ , *Chemphyschem* 13 (2012) 3651–3654.
- [22] C.H. Hendon, D. Tiana, M. Fontecave, C. Sanchez, L. D'arras, C. Sasse, L. Rozes, C. Mellot-Draznieks, A. Walsh, Engineering the optical response of the Titanium-MIL-125 metal-organic framework through ligand functionalization, *J. Am. Chem. Soc.* 135 (2013) 10942–10945.
- [23] J. Resasco, H. Zhang, N. Kornienko, N. Becknell, H. Lee, J. Guo, A.L. Briseno, P. Yang,  $\text{TiO}_2/\text{BiVO}_4$  nanowire heterostructure photoanodes based on Type II band alignment, *ACS Cent. Sci.* 2 (2016) 80–88.
- [24] Y. Yin, Z. Jin, F. Hou, Enhanced solar water-splitting efficiency using core/sheath heterostructure  $\text{CdS}/\text{TiO}_2$  nanotube arrays, *Nanotechnology* 18 (2007) 495608.
- [25] R.M. Abdelhameed, M.M. Simoes, A.M. Silva, J. Rocha, Enhanced photocatalytic activity of MIL-125 by post-synthetic modification with  $\text{Cr}(\text{III})$  and Ag nanoparticles, *Chemistry* 21 (2015) 11072–11081.
- [26] M.M. Walczak, D.A. Dryer, D.D. Jacobson, M.G. Foss, N.T. Flynn, pH dependent redox couple: an illustration of the Nernst equation, *J. Chem. Educ.* 74 (1997) 1195.
- [27] Z. Chen, T.F. Jaramillo, T.G. Deutsch, A. Kleiman-Shwarstein, A.J. Forman, N. Gaillard, R. Garland, K. Takanabe, C. Heske, M. Sunkara, E.W. McFarland, K. Domen, E.L. Miller, J.A. Turner, H.N. Dinh, Accelerating materials development for photoelectrochemical hydrogen production: standards for methods, definitions, and reporting protocols, *J. Mater. Res.* 25 (2011) 3–16.
- [28] H. Dotan, K. Sivula, M. Grätzel, A. Rothschild, S.C. Warren, Probing the photoelectrochemical properties of hematite ( $\alpha\text{-Fe}_2\text{O}_3$ ) electrodes using hydrogen peroxide as a hole scavenger, *Energy Environ. Sci.* 4 (2011) 958–964.
- [29] H. Wang, Y. Bai, Q. Wu, W. Zhou, H. Zhang, J. Li, L. Guo, Rutile  $\text{TiO}_2$  nano-branched arrays on FTO for dye-sensitized solar cells, *Phys. Chem. Chem. Phys.* 13 (2011) 7008–7013.
- [30] M. Abd-Lefdil, R. Diaz, H. Bihri, M.A. Aouaj, F. Rueda, Preparation and characterization of sprayed FTO thin films, *Eur. Phys. J.-Appl. Phys.* 38 (2007) 217–219.
- [31] C.J. Howard, T.M. Sabine, F. Dickson, Structural and thermal parameters for rutile and anatase, *Acta Crystallogr. B* 47 (1991) 462–468.
- [32] B. Liu, E.S. Aydil, Growth of oriented single-crystalline rutile  $\text{TiO}_2$  nanorods on transparent conducting substrates for dye-sensitized solar cells, *J. Am. Chem. Soc.* 131 (2009) 3985–3990.
- [33] Y. Ling, J.K. Cooper, Y. Yang, G. Wang, L. Munoz, H. Wang, J.Z. Zhang, Y. Li, Chemically modified titanium oxide nanostructures for dye-sensitized solar cells, *Nano Energy* 2 (2013) 1373–1382.
- [34] W.-Q. Fan, X.-Q. Yu, S.-Y. Song, H.-Y. Bai, C. Zhang, D. Yan, C.-B. Liu, Q. Wang, W.-D. Shi, Fabrication of  $\text{TiO}_2\text{-BiOCl}$  double-layer nanostructure arrays for photoelectrochemical water splitting, *CrystEngComm* 16 (2014) 820–825.
- [35] Y.J. Hwang, C. Hahn, B. Liu, P. Yang, Photoelectrochemical properties of  $\text{TiO}_2$  nanowire arrays: a study of the dependence on length and atomic layer deposition coating, *ACS Nano* 6 (2012) 5060–5069.
- [36] M. Dan-Hardi, C. Serre, T. Frot, L. Rozes, G. Maurin, C. Sanchez, G. Férey, A new photoactive crystalline highly porous Titanium(IV) dicarboxylate, *J. Am. Chem. Soc.* 131 (2009) 10857–10859.
- [37] J.G. Santaclara, M.A. Nasalevich, S. Castellanos, W.H. Evers, F.C.M. Spoor, K. Rock, L.D.A. Siebbeles, F. Kapteijn, F. Grozema, A. Houtepen, J. Gascon, J. Hunger, M.A. van der Veen, Organic linker defines the excited-state decay of photocatalytic MIL-125(Ti)-type materials, *ChemSuschem* 9 (2016) 388–395.
- [38] M.A. Nasalevich, C.H. Hendon, J.G. Santaclara, K. Svane, B. van der Linden, S.L. Veber, M.V. Fedin, A.J. Houtepen, M.A. van der Veen, A. Walsh, J. Gascon, Electronic origins of photocatalytic activity in  $d_0$  metal organic frameworks, *Sci. Rep.-UK* 6 (2016).
- [39] U. Shaislamov, B.L. Yang, Single crystalline  $\text{TiO}_2$  nanorods with enhanced visible light activity for solar hydrogen generation, *Int. J. Hydrogen Energy* 38 (2013) 14180–14188.
- [40] X.M. Sun, Q. Sun, Q. Zhang, Q.Q. Zhu, H.Z. Dong, L.F. Dong, Significant effects of reaction temperature on morphology, crystallinity, and photoelectrical properties of rutile  $\text{TiO}_2$  nanorod array films, *J. Phys. D Appl. Phys.* 46 (2013).
- [41] H. Wang, X.Z. Yuan, Y. Wu, G.M. Zeng, X.H. Chen, L.J. Leng, Z.B. Wu, L.B. Jiang, H. Li, Facile synthesis of amino-functionalized titanium metal-organic frameworks and their superior visible-light photocatalytic activity for  $\text{Cr}(\text{VI})$  reduction, *J. Hazard. Mater.* 286 (2015) 187–194.
- [42] B. Sun, T. Shi, Z. Peng, W. Sheng, T. Jiang, G.J.N.R.L. Liao, Controlled fabrication of  $\text{Sn}/\text{TiO}_2$  nanorods for photoelectrochemical water splitting, *Nanoscale Res. Lett.* 8 (2013) 462.
- [43] Y. Fu, H. Yang, R. Du, G. Tu, C. Xu, F. Zhang, M. Fan, W. Zhu, Enhanced photocatalytic  $\text{CO}_2$  reduction over Co-doped  $\text{NH}_2\text{-MIL}-125(\text{Ti})$  under visible light, *RSC Adv.* 7 (2017) 42819–42825.
- [44] X. Li, Y. Pi, Q. Hou, H. Yu, Z. Li, Y. Li, J. Xiao, Amorphous  $\text{TiO}_2/\text{NH}_2\text{-MIL}-125(\text{Ti})$  homologous MOF-encapsulated heterostructures with enhanced photocatalytic activity, *Chem. Commun. (Camb.)* 54 (2018) 1917–1920.
- [45] H. Liu, J. Zhang, D. Ao, Construction of heterostructured  $\text{ZnIn}_2\text{S}_4/\text{NH}_2\text{-MIL}-125(\text{Ti})$  nanocomposites for visible-light-driven  $\text{H}_2$  production, *Appl. Catal. B: Environ.* 221 (2018) 433–442.
- [46] D.Q. Jin, A.Q. Gong, H. Zhou, Visible-light-activated photoelectrochemical biosensor for the detection of the pesticide acetochlor in vegetables and fruit based on its inhibition of glucose oxidase, *RSC Adv.* 7 (2017) 17489–17496.
- [47] D.K. Zhong, S. Choi, D.R. Gamelin, Near-complete suppression of surface recombination in solar photoelectrolysis by “Co-Pi” catalyst-modified  $\text{W:BiVO}_4$ , *J. Am. Chem. Soc.* 133 (2011) 18370–18377.
- [48] P.M. Rao, L. Cai, C. Liu, I.S. Cho, C.H. Lee, J.M. Weisse, P. Yang, X. Zheng, Simultaneously efficient light absorption and charge separation in  $\text{WO}_3/\text{BiVO}_4$  core/shell nanowire photoanode for photoelectrochemical water oxidation, *Nano Lett.* 14 (2014) 1099–1105.
- [49] L. Zhou, C. Zhao, B. Giri, P. Allen, X. Xu, H. Joshi, Y. Fan, L.V. Titova, P.M. Rao, High light absorption and charge separation efficiency at low applied voltage from Sb-doped  $\text{SnO}_2/\text{BiVO}_4$  core/shell nanorod-array photoanodes, *Nano Lett.* 16 (2016) 3463–3474.
- [50] M.B. Chambers, X. Wang, L. Ellezam, O. Ersen, M. Fontecave, C. Sanchez, L. Rozes, C. Mellot-Draznieks, Maximizing the photocatalytic activity of metal-organic frameworks with aminated-functionalized linkers: substoichiometric effects in  $\text{MIL}-125\text{-NH}_2$ , *J. Am. Chem. Soc.* 139 (2017) 8222–8228.